The Astrophysical Journal, 715:651–655, 2010 May 20 doi:10.1088/0004-637X/715/1/651

G-BAND AND HARD X-RAY EMISSIONS OF THE 2006 DECEMBER 14 FLARE OBSERVED BY *HINODE*/SOT AND *RHESSI*

Kyoko Watanabe[1], Säm Krucker[2], Hugh Hudson[2], Toshifumi Shimizu[1], Satoshi Masuda[3], and Kiyoshi Ichimoto[4]
[1] Institute of Space and Astronautical Science, Japan Aerospace Exploration Agency, 3-1-1 Yoshinodai, Chuo-ku, Sagamihara, Kanagawa 252-5210, Japan; watanabe.kyoko@isas.jaxa.jp
[2] Space Sciences Laboratory, University of California at Berkeley, 7 Gauss Way, Berkeley, CA 94720-7450, USA
[3] Solar-Terrestrial Environment Laboratory, Nagoya University, Furo-cho, Chikusa-ku, Nagoya 464-8601, Japan
[4] Kwasan and Hida Observatories, Kyoto University, Yamashina, Kyoto 607-8471, Japan
Received 2009 September 3; accepted 2010 April 10; published 2010 April 30

ABSTRACT

We report on *G*-band emission observed by the Solar Optical Telescope on board the *Hinode* satellite in association with the X1.5-class flare on 2006 December 14. The *G*-band enhancements originate from the footpoints of flaring coronal magnetic loops, coinciding with nonthermal hard X-ray bremsstrahlung sources observed by the *Reuven Ramaty High Energy Solar Spectroscopic Imager*. At the available 2 minute cadence, the *G*-band and hard X-ray intensities are furthermore well correlated in time. Assuming that the *G*-band enhancements are continuum emission from a blackbody, we derived the total radiative losses of the white-light flare (white-light power). If the *G*-band enhancements additionally have a contribution from lines, the derived values are overestimates. We compare the white-light power with the power in hard X-ray producing electrons using the thick-target assumption. Independent of the cutoff energy of the accelerated electron spectrum, the white-light power and the power of accelerated electrons are roughly proportional. Using the observed upper limit of ∼30 keV for the cutoff energy, the hard X-ray producing electrons provide at least a factor of 2 more power than needed to produce the white-light emission. For electrons above 40 keV, the powers roughly match for all four of the time intervals available during the impulsive phase. Hence, the flare-accelerated electrons contain enough energy to produce the white-light flare emissions. The observed correlation in time, space, and power strongly suggests that electron acceleration and white-light production in solar flares are closely related. However, the results also call attention to the inconsistency in apparent source heights of the hard X-ray (chromosphere) and white-light (upper photosphere) sources.

Key words: Sun: chromosphere – Sun: flares – Sun: particle emission – Sun: photosphere – Sun: X-rays, gamma rays

Online-only material: color figures

1. INTRODUCTION

In association with solar flares, we sometimes observe enhancements of visible continuum, in which case the event is termed a "white-light flare." Although white-light events had previously been mainly associated with energetic flares (*GOES* X-class), there are now reports of continuum emission from events as weak as C-class flares (Matthews et al. 2003; Hudson et al. 2006; Wang 2009; Jess et al. 2008) thanks to accurate photometry from space achieved by *Yohkoh*, *TRACE*, and *Hinode,* and by improved ground-based instruments. However, white-light flares are still very infrequently observed and some energetic events do not show any enhancement in white light. The processes causing it remain unclear (Neidig 1989). Because there is a good correlation of light curves and sites of emission between optical continuum and hard X-rays (e.g., Rust & Hegwer 1975; Neidig 1989; Hudson et al. 1992; Metcalf et al. 2003; Xu et al. 2006), there is some consensus that the origin of white-light emission lies in the energy in accelerated particles, especially nonthermal electrons.

Using the thick-target model (Brown 1971), the energy in flare-accelerated electrons can be compared to the radiative losses in white light (e.g., Hudson 1972). If flare-accelerated electrons indeed produce the white-light emission, the energy content in electrons must be larger than the radiative losses in white light. Due to the (inferred) steep electron spectrum, the energy in electrons strongly depends on the cutoff of the electron spectrum at low energies. To match the energies, Neidig (1989) and Ding et al. (2003) estimated the cutoff energy of electrons at more than 50 keV, whereas Fletcher et al. (2007) obtained values below 25 keV from a statistical analysis of *Transition Region and Coronal Explorer* (*TRACE*) and *Reuven Ramaty High Energy Solar Spectroscopic Imager* (*RHESSI*) observations. These differences might be due to the variation from flare to flare. In any case, a cutoff energy of ∼20 keV can supply the white-light power, but not 100 keV.

The Solar Optical Telescope (SOT) of *Hinode* (Tsuneta et al. 2008; Suematsu et al. 2008; Shimizu et al. 2008; Ichimoto et al. 2008) makes observations in white light. Its broadband filter imager (BFI) takes images in red (668.40 nm, width 0.4 nm), green (555.05 nm, width 0.4 nm), and blue (450.45 nm, width 0.4 nm) continuum ranges. Radiation at these wavelengths comes from the photosphere and hence reflects the broadband continuum emission well. However, SOT normally obtains only infrequent images in these filters. More frequently, SOT takes images in the *G* band (430.50 nm, width 0.83 nm), formed mainly from CH line opacity. Carlsson et al. (2007) show contribution functions for these filters; the *G* band has a photospheric and an upper-photospheric contribution. It therefore serves well to define the morphology of white-light flares, and it was also used in the *Yohkoh* observations (Hudson et al. 1992; Matthews et al. 2003). However, *G*-band emission could contain not only continuum emission, but also CH line emission. If the *G*-band emission contains line emission, the radiative losses estimated from the *G*-band emission assuming blackbody radiation are overestimates of the true losses. However, in this paper, we treat

the *G*-band emission mainly came from the continuum emission, and we therefore use *G*-band images as a proxy for the white-light images.

SOT observed white-light emission from three X-class flares in 2006 December (Wang 2009). *G*-band emission of the largest event (X3.4 flare on 2006 December 13) is reported by Isobe et al. (2007) and Jing et al. (2008). Isobe et al. (2007) concluded that the white-light emission could be produced by radiative back-warming resulting from particle-beam heating, and Jing et al. (2008) noted that the white-light emissions appeared at the sites of the largest inferred reconnection rates. In this paper, we describe the white-light observations of the 2006 December 14 flare that was also observed by the *RHESSI* (Lin et al. 2002). We obtain X-ray energy spectra for each footpoint separately, using *RHESSI* imaging spectroscopy, and compare the results with energy estimated from *Hinode* *G*-band images (Section 2). In Section 3, energy estimates are discussed for different cutoff energies.

2. OBSERVATIONS BY *HINODE*/SOT AND *RHESSI*

On 2006 December 14, an X1.5-class flare occurred in active region NOAA 10930; this region produced a total of three X-class flares in 2006 December. *Hinode*/SOT took *G*-band images every 2 minutes, obtaining four images between 22:09 and 22:16 UT that showed flare-related brightenings. The exposure times of these images were 0.031 s, and the spatial binning was $0\farcs109$ pixels^{-1}. To estimate the excess emission from these images, we made a reference image by averaging images before (22:07 UT) and after (22:17 UT), and subtracted the reference from the flare images. We then calculated background pixel statistics for these difference images and estimated the excess emission by summing the pixels at more than 3σ (= 245.3 DN/exposure time/pixel) above the background level. *RHESSI* had full coverage of this flare. Figure 1 shows light curves from *GOES* X-rays, *G*-band emission by *Hinode*/SOT obtained as described above, and hard X-rays observed by *RHESSI*. The total white-light emission correlates well with hard X-rays at 40–100 keV, as shown in the fourth panel of Figure 1. Note that the white-light images are brief samples, whereas the hard X-ray record is continuous.

Around the time of the *Hinode* images, we made *RHESSI* hard X-ray images integrated over 1 minute by using the CLEAN algorithm with sub-collimators 2, 3, 4, 6, 8, and 9. Despite its lower energy resolution, sub-collimator 2 is used here to obtain higher spatial resolution for images reconstructed over a broad energy range. Sub-collimator 5 is affected by cumulative radiation damage and is therefore not used (the observations presented here were taken before the first *RHESSI* anneal). It is necessary to register the *RHESSI* and *Hinode* images empirically. For this purpose, we compared *RHESSI* thermal X-ray images at 6 keV with images from *Hinode*/X-ray telescope (XRT) and shifted the latter to fit. The alignment between SOT/*G* band and XRT was corrected by using the method described in Shimizu et al. (2007). The results for this registration are shown in the top figures of Figures 2–5. Above 40 keV, the hard X-ray images show two footpoint sources, with the *G*-band emission at the same locations within uncertainties. The hard X-ray footpoint regions have different spectral behavior; the 20–30 keV energy range shows the northwest (NW) source more clearly than the southeast (SE) one. The behavior in white light is opposite to this, i.e., the SE region is brighter. On the other hand, if we use 40–100 keV hard X-rays, a similar feature

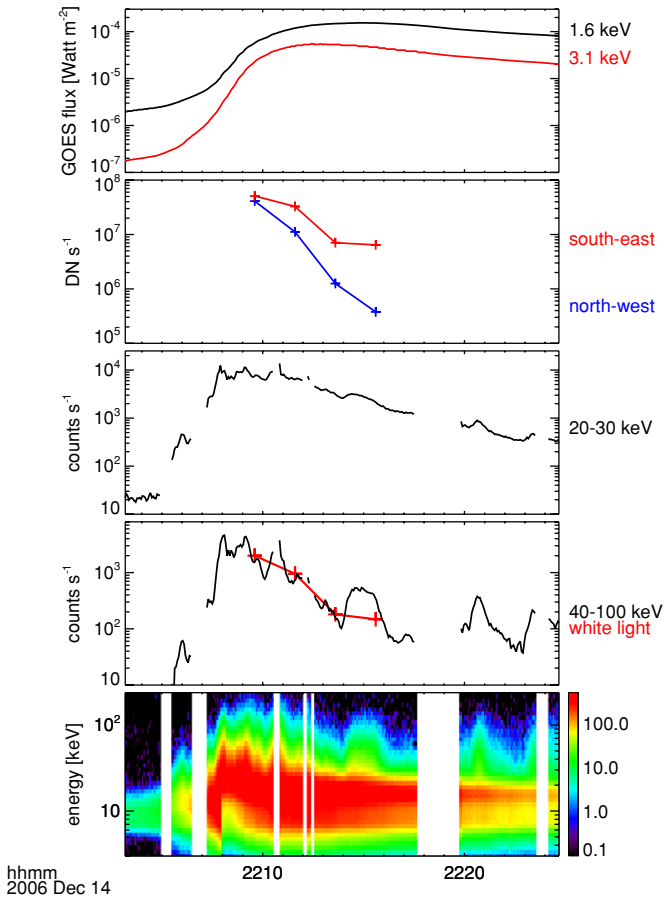

Figure 1. Light curves of *GOES* soft X-rays, *G*-band excess emission from *Hinode*/SOT, and 20–30 and 40–100 keV range hard X-ray emissions from *RHESSI*. The bottom panel is a *RHESSI* spectrogram, and the color bar on the right shows the spectral flux (counts/4 s). Total white-light emission (sum of SE and NW emissions at each image time) is overlaid on the hard X-ray light curve in the next-to-bottom panel, showing a good correlation.

(A color version of this figure is available in the online journal.)

of the white-light emission was obtained. This SE feature was seen clearly in all four images at 40–100 keV.

We derived energy spectra of each footpoint separately by obtaining images at different energy bands (e.g., Krucker & Lin 2002). For the first time interval, the spectrum for both footpoints could be derived showing similar power-law spectra (Figure 2). For the later time intervals, the NW footpoint is too weak to accurately determine its spectrum, and only the spectrum of the SE footpoint is derived (Figures 2–5).

3. RELATIONSHIP BETWEEN WHITE-LIGHT AND HARD X-RAY EMISSIONS

In this section, the power of the white-light continuum (radiative losses) is compared with the energy deposition by flare-accelerated electrons producing the hard X-ray emission. The white-light power is calculated assuming that the *G*-band enhancements are continuum emission from a blackbody. This is a strong assumption that is not necessarily fulfilled. Besides the continuum emission, the *G*-band emission could contain line emission. In this case, our assumption leads to an overestimation of the white-light power. A further limitation of our assumption is that the spectrum of the white-light flare emission could be different from a blackbody. We further assume temperatures of 6000 K for the quiet Sun, 5500 K for the penumbral

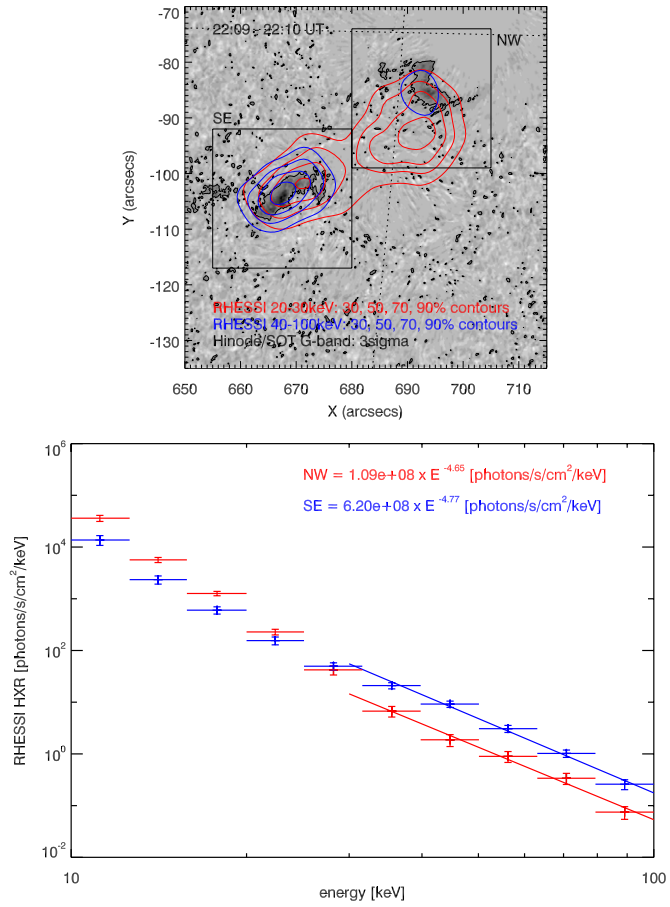

Figure 2. Top: image of *G*-band emission taken by *Hinode*/SOT and *RHESSI* hard X-ray contours at 22:09 UT. The background image is the differential *G*-band image (the average of the images taken at 22:07 UT and 22:17 UT is subtracted), and the black contours indicate 3σ above background. Red contours show 20–30 keV emission, and blue contours show 40–100 keV emission. The black box gives the area over which the *RHESSI* image is searched for emission from the footpoint. Only emission above 3σ is added to derive the spectrum. Bottom: photon spectra for each footpoint at 22:09 UT. The red crosses and lines indicate spectra in the NW box, and blue ones indicate spectra in the SE box, with 1σ error bars. Energy bands of the spectrum were in a logarithmic space, and each spectrum was fitted in the range above 30 keV.

(A color version of this figure is available in the online journal.)

regions, and 4200 K for the umbra (e.g., Cox 2000), and calculate the temperature of the white-light flare source using the response of the *G*-band filter and Planck's law ($B_\lambda(T) = 2hc^2/\lambda^5(e^{hc/\lambda kT} - 1)$). The power of the white-light continuum E (i.e., radiative losses) from the temperature T_e is then calculated using Stefan–Boltzmann's law ($E = 5.67 \times 10^{-8}\ T_e^4$). Note that this represents a lower limit because the continuum could extend into the UV, e.g., via the Balmer continuum (e.g., Fletcher et al. 2007).

The total power in nonthermal electrons P above a given cutoff energy ε_c in the thick-target approximation (Equation (1); Hudson et al. 1978) can be derived from the observed hard X-ray photon spectrum $I(\epsilon_x)$ (as shown in Figures 2–5):

$$P(\varepsilon \geqslant \varepsilon_c) = 4.3 \times 10^{24} \frac{b(\gamma)}{\gamma - 1} A\, \varepsilon_c^{-(\gamma-1)} \quad (\text{erg s}^{-1}), \quad (1)$$

$$I(\epsilon_x) = A\, \epsilon_x^{-\gamma} \quad (\text{photons cm}^{-2}\ \text{s}^{-1}\ \text{keV}^{-1}). \quad (2)$$

The factor $b(\gamma)$ is an auxiliary function from Brown (1971) as calculated by Hudson et al. (1978) for a relevant range of

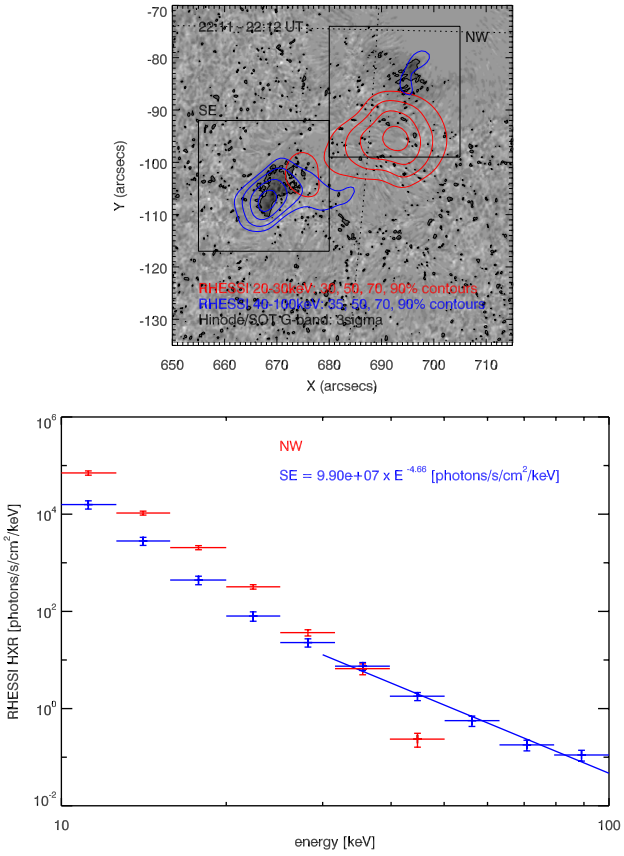

Figure 3. Same as in Figure 2 for 22:11 UT.

(A color version of this figure is available in the online journal.)

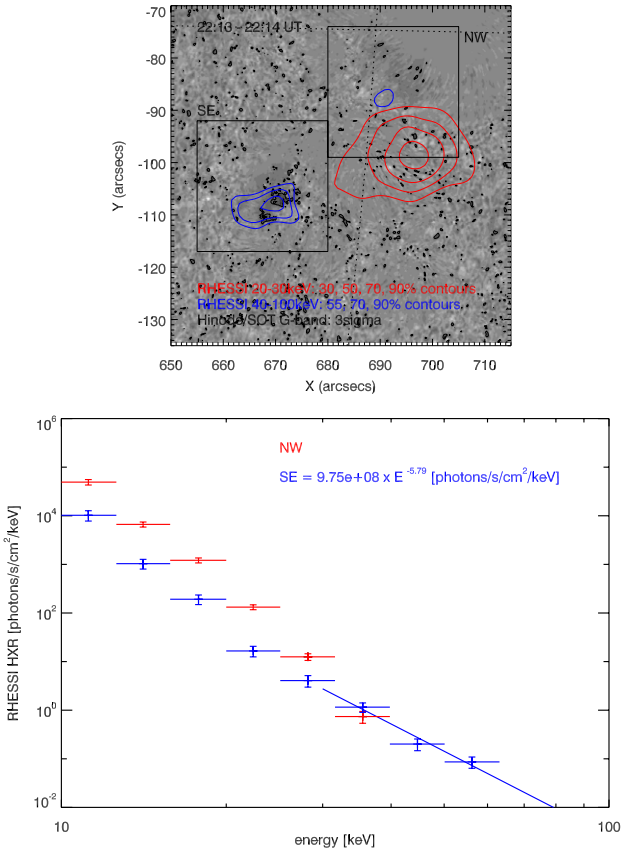

Figure 4. Same as in Figure 2 for 22:13 UT.

(A color version of this figure is available in the online journal.)

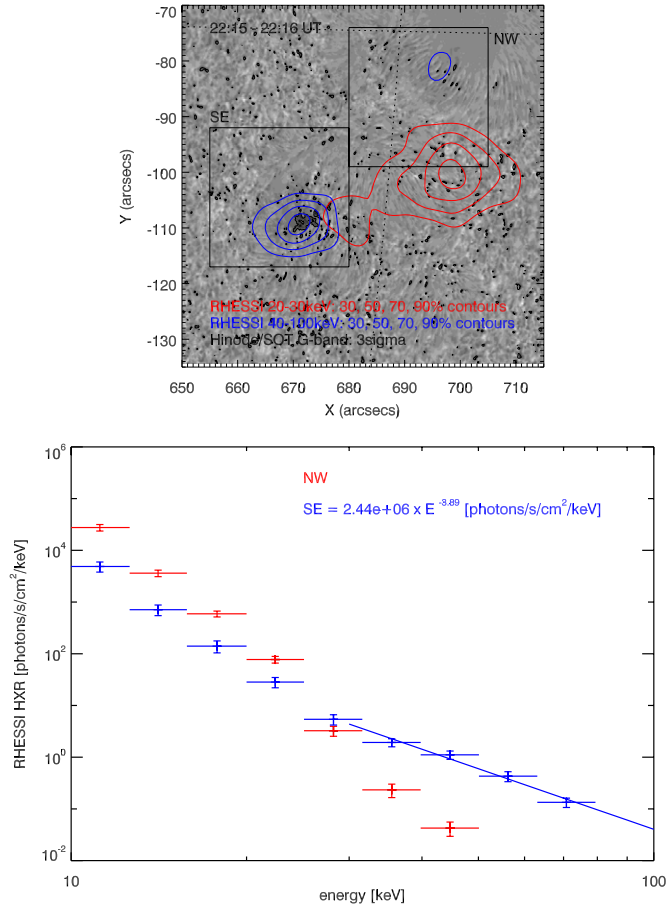

Figure 5. Same as in Figure 2 for 22:15 UT.
(A color version of this figure is available in the online journal.)

spectral indices γ as $b(\gamma) \approx 0.27\gamma^3$. Two approaches to derive P are presented: first, P is estimated from the total flare spectrum integrated over 4 s around the time of the *G*-band image (Figure 6). Second, P is estimated for each footpoint source separately using imaging spectroscopy (Figures 2–5 and 7). The advantage of the first approach is that it provides smaller uncertainties and that the *RHESSI* images are taken almost simultaneously with the *G*-band images (cf. Figure 1). The second approach compares individual sources, but a time integration of 60 s is needed to obtain a significant result. However, both approaches give similar results (Figures 6 and 7). Error bars are estimated from the uncertainties of the fit parameters. The uncertainty in δ (typically ~5% for the spatially integrated spectra and 10% for imaging spectroscopy; Krucker & Lin 2002) dominates the error budget. There is a clear correlation between the power in white-light emissions and the energy deposition rate by nonthermal electrons for all cutoff energies. For low cutoff energies, the power provided by nonthermal electrons is well above the white-light power (e.g., ~50% of the power in electrons above 30 keV is enough to account for the white-light emission). The total power of electrons above ~40 keV roughly matches the white-light power. If the *G*-band emission contains not only continuum emission but also line emission, the values for the white-light power derived above are overestimates. In any case, for all realistic cutoff energies, the energy in nonthermal electrons (derived from thick-target assumptions) is larger than the white-light power, and independent of values of the cutoff energies, the derived powers are correlated.

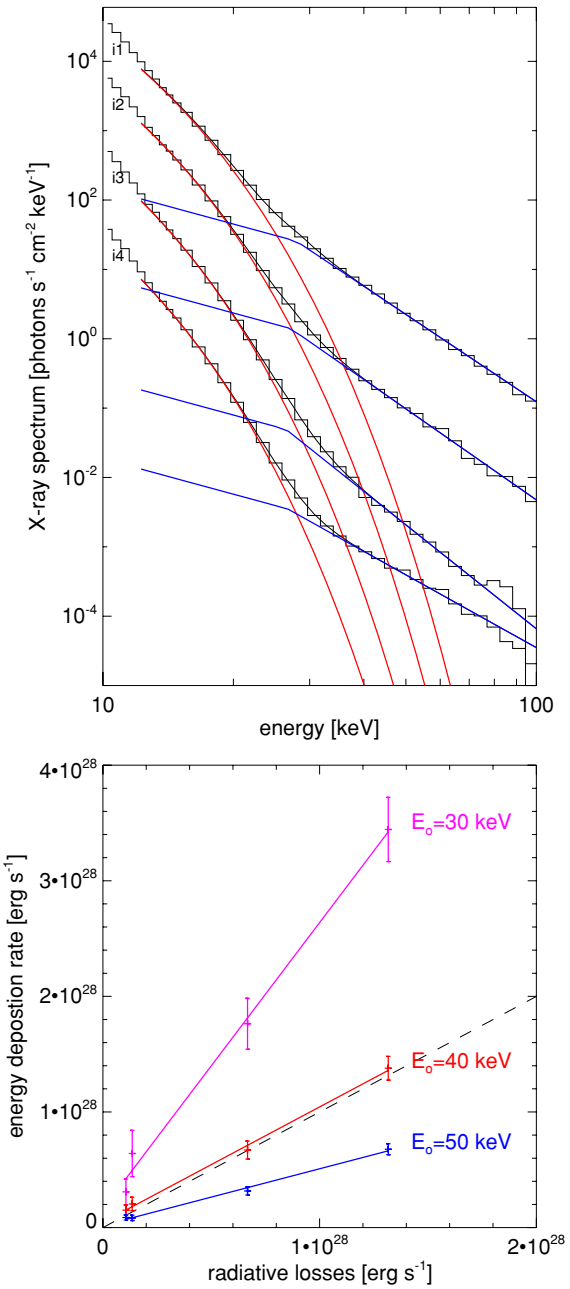

Figure 6. Top: hard X-ray photon spectra integrated over 4 s around the time of the four *G*-band images. The black histogram represents the data. The red and blue curves are a thermal and broken power-law fit to the data, while the black curve represents the sum of the two fits. Spectra from later intervals are successively divided by an additional factor of 10 for a clearer representation. Bottom: correlation plot of total power in white-light continuum (radiative losses) and the derived power in nonthermal electrons for different cutoff energies as indicated. The four data points correspond to the four time intervals and are connected by lines to indicate time evolution. The dashed line outlines equality between energy deposition rate and radiative losses.
(A color version of this figure is available in the online journal.)

4. DISCUSSION AND SUMMARY

The observations discussed in this paper show that the solar flare white-light emission is closely related in time, space, and power to the acceleration of nonthermal electrons. To explain the observed correlation between white light and high-energy hard X-ray emission in the simplest possible way, the two components should originate in the same source region. Continuum emission in the *G*-band emission comes from

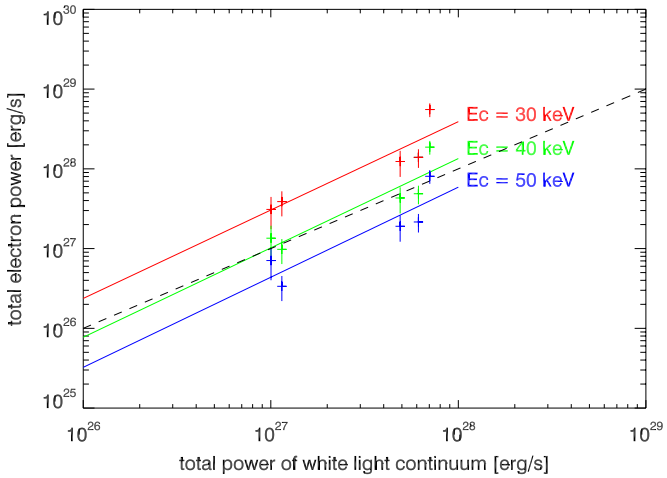

Figure 7. Same plot as in Figure 6 (bottom) derived from imaging spectroscopy results. The shown data points correspond to the NW footpoint (first interval only; dynamic range of hard X-ray images is too low to derive accurate values for later intervals) and the SE footpoint (all intervals) as shown in the images of Figures 2–5. The different colors correspond to different cutoff energies as indicated.

(A color version of this figure is available in the online journal.)

0–100 km above the photosphere (see Figure 1 of Carlsson et al. 2007), and hard X-ray emission in 50–100 keV originates in the chromosphere. Observationally, the emission site of 50–100 keV hard X-rays is estimated at 6.5×10^3 km height above the photosphere from (early) *Yohkoh* observations (Matsushita et al. 1992) and around 600 km height by *RHESSI* for a single event (Kontar et al. 2008). This information is weak, and we would like to see systematic *RHESSI* data analyses on this point, but the existing data suggest a difference of more than 500 km between the emission sites (Kontar et al. 2008; Carlsson et al. 2007). Theoretically, a 50–100 keV electron should thermalize some 1000 km height above the photosphere; at this mid-chromospheric height, the density is about $10^{13.5}$ cm^{-3} (Neidig 1989). At these energies, however, the electrons cannot penetrate into the lower chromosphere, and thus they do not heat the photosphere. Electron energies more than 900 keV are necessary for penetration to the photosphere, even if the flare site has become ionized (Neidig 1989). However, the energy in 900 keV electrons is far too small (by about 4 orders of magnitude, assuming the power law seen at 40 keV can be extrapolated to 900 keV) to produce the white-light emission. The data presented here therefore call attention to the need for a white-light emission model which can explain the good correlation with high-energy electron emission and difference of the emission height of white light and hard X-rays. Nonthermal ionization levels enhance the continuum (Hudson 1972) and also make back-warming possible (e.g., Metcalf et al. 2003), but we do not have well-defined models for these processes in realistic physical conditions yet.

Hinode is a Japanese mission developed and launched by ISAS/JAXA, collaborating with NAOJ as a domestic partner, NASA and STFC (UK) as international partners. Scientific operation of the *Hinode* mission is conducted by the *Hinode* science team organized at ISAS/JAXA. This team mainly consists of scientists from institutes in the partner countries. Support for the post-launch operation is provided by JAXA and NAOJ (Japan), STFC (UK), NASA, ESA, and NSC (Norway). *RHESSI* is the NASA Small Explorer mission; we appreciate the *RHESSI* team for their support to the mission and guidance in the analysis of the *RHESSI* satellite data. Authors Hudson and Krucker thank NASA for support under grant NAS 5-98033. A part of this work was carried out by the joint research program of the Solar-Terrestrial Environment Laboratory, Nagoya University. We also appreciate fruitful comments from an anonymous referee.

REFERENCES

Brown, J. C. 1971, Sol. Phys., 18, 489
Carlsson, M., et al. 2007, PASJ, 59, S663
Cox, A. N. 2000, Allen's Astrophysical Quantities (New York: Springer)
Ding, M. D., Liu, Y., Yeh, C.-T., & Li, J. P. 2003, A&A, 403, 1151
Fletcher, L., Hannah, I. G., Hudson, H. S., & Metcalf, T. R. 2007, ApJ, 656, 1187
Hudson, H. S. 1972, Sol. Phys., 24, 414
Hudson, H. S., Acton, L. W., Hirayama, T., & Uchida, Y. 1992, PASJ, 44, L77
Hudson, H. S., Canfield, R. C., & Kane, S. R. 1978, Sol. Phys., 60, 137
Hudson, H. S., Wolfson, C. J., & Metcalf, T. R. 2006, Sol. Phys., 234, 79
Ichimoto, K., et al. 2008, Sol. Phys., 249, 233
Isobe, H., et al. 2007, PASJ, 59, S807
Jess, D. B., Mathioudakis, M., Crockett, P. J., & Keenan, F. P. 2008, ApJ, 688, L119
Jing, J., Chae, J., & Wang, H. 2008, ApJ, 672, L73
Kontar, E. P., Hannah, I. G., & MacKinnon, A. L. 2008, A&A, 489, L57
Krucker, S., & Lin, R. P. 2002, Sol. Phys., 210, 229
Lin, R. P., et al. 2002, Sol. Phys., 210, 3
Matsushita, K., Masuda, S., Kosugi, T., Inda, M., & Yaji, K. 1992, PASJ, 44, L89
Matthews, S. A., van Driel-Gesztelyi, L., Hudson, H. S., & Nitta, N. V. 2003, A&A, 409, 1107
Metcalf, T. R., Alexander, D., Hudson, H. S., & Longcope, D. W. 2003, ApJ, 595, 483
Neidig, D. F. 1989, Sol. Phys., 121, 261
Rust, D. M., & Hegwer, F. 1975, Sol. Phys., 40, 141
Shimizu, T., et al. 2007, PASJ, 59, S845
Shimizu, T., et al. 2008, Sol. Phys., 249, 221
Suematsu, Y., et al. 2008, Sol. Phys., 249, 197
Tsuneta, S., et al. 2008, Sol. Phys., 249, 167
Veronig, A. M., & Brown, J. C. 2004, ApJ, 603, 117
Wang, H. 2009, Res. Astron. Astrophys., 9, 127
Xu, Y., et al. 2006, ApJ, 641, 1210